

Improved k-means and spectral matching for hyperspectral mineral mapping

Zhongliang Ren^a, Lin Sun^{a,*}, Qiuping Zhai^b



^aCollege of Geodesy and Geomatics, Shandong University of Science and Technology, Qingdao 266590, China

^bShandong Provincial Key Laboratory of Water and Soil Conservation and Environmental Protection, College of Resources and Environment, Linyi University, Linyi 276000, China

ARTICLE INFO

Keywords:

Hyperspectral mineral mapping
Improved k-means
Similarity measurement method
Spectral absorption feature
Spectral matching

ABSTRACT

Mineral mapping is an important step for the development and utilization of mineral resources. The emergence of remote sensing technology, especially hyperspectral imagery, has paved a new approach to geological mapping. The k-means clustering algorithm is a classical approach to classifying hyperspectral imagery, but the influence of mixed pixels and noise mean that it usually has poor mineral mapping accuracy. In this study, the mapping accuracy of the k-means algorithm was improved in three ways: similarity measurement methods that are insensitive to dimensions are used instead of the Euclidean distance for clustering; the spectral absorption features of minerals are enhanced; and the mineral mapping results are combined as the number of cluster centers (K) is incremented from 1. The improved algorithm is used with combined spectral matching to match the clustering results with a spectral library. A case study on Cuprite, Nevada, demonstrated that the improved k-means algorithm can identify most minerals with the kappa value of over 0.8, which is 46% and 15% higher than the traditional k-means and spectral matching technology. New mineral types are more likely to be found with increasing K . When K is much greater than the number of mineral types, the accuracy is improved, and the mineral mapping results are independent of the similarity measurement method. The improved k-means algorithm can also effectively remove speckle noise from the mineral mapping results and be used to identify other objects.

1. Acronyms

Category	Acronyms	Full name
Clustering parameters	K	The number of cluster centers
Similarity measurement methods	ED	Euclidean distance
	SAM	Spectral angle mapper
	SCC	Spectral correlation coefficient
Spectral features	OS	Original spectrum
	ER	Envelope removal
	BD	Band depth
Mineral mapping methods	CSM	Combined spectral matching
	SKM	The k-means when $K = 6$
	EKM	The k-means when the iteration ends
	CKM	The improved k-means proposed in this paper
Mineral mapping results	PMMR	The previous mineral mapping result
	CMMR	The current mineral mapping result
Accuracy indexes	DBI	Davies-Bouldin index
	OA	Overall accuracy
	KC	Kappa coefficient
Filtering methods	HWF	Hamming window filter

2. Introduction

Mineral resources, especially altered minerals, have played an important role in human survival and development because of their economic and scientific implications. For example, kaolinite is a well-known altered mineral that is usually used as ceramic materials (Ouahabi et al., 2014) and andalusite can be used in the refractory industry to provide thermal shock resistance and strong mechanical properties (Kakroudji et al., 2009). Mapping these mineral resources is a prerequisite for their utilization. The exploration of porphyry copper, epithermal gold, massive sulfide and uranium deposits all depends on the mineral mapping of hydrothermal alteration zones (Pour and Hashim, 2011, Pour and Hashim, 2015a, Pour and Hashim, 2015b; Craw et al., 2009; Bhadra et al., 2013). In addition, hydrothermal alteration mapping can also be used to evaluate the characteristics of the geothermal systems (Abubakar et al., 2018; Mauriohooho et al., 2016) and delineate areas vulnerable to toxic metal contamination (Moore et al., 2008).

Traditional mineral mapping methods involve two steps (Fisher, 1998): geologists visually identify minerals according to their physical

* Corresponding author.

E-mail address: sunlin6@126.com (L. Sun).

appearance and properties in the field, and instruments and drugs are used in the laboratory for analysis and identification. Large-scale application of such methods can be time-consuming and laborious. Hyperspectral remote sensing was first proposed by Hunt (1979), who was studying the spectral properties of minerals. One of the most successful applications of hyperspectral remote sensing has been geological mapping (Vane and Goetz, 1993). Mineral mapping of hyperspectral images mainly depends on the diagnostic spectral features of minerals (Meer, 2004). Hyperspectral remote sensing allows continuous sampling from the visible to short-wave infrared spectra, so it is quicker and more effective at mineral mapping than traditional mineral mapping methods and multispectral remote sensing (Kruse et al., 2003; Vaughan et al., 2003).

Various mineral mapping methods based on hyperspectral images have been developed over the years, including supervised classification, spectral unmixing, decision tree, and spectral matching. Supervised classification can improve the mineral mapping accuracy by repeated checking of the training samples (Abedi et al., 2011). However, the selection and evaluation of training samples are time-consuming. Spectral unmixing can obtain the ratios of different minerals in the same pixel (Kruse et al., 1993b). The determination of end-element spectra, which is the key step to spectral unmixing, usually assumes that there are pure end-elements in the image. However, this assumption is untenable because of the low spatial resolution of hyperspectral images. The decision tree method usually realizes mineral mapping by setting thresholds for spectral absorption parameters (Wei et al., 2015). Although this method makes full use of the spectral feature differences between minerals, the selection of thresholds needs a large number of experiments, and the selected thresholds are generally not applicable to different hyperspectral sensors. While these three methods all require prior knowledge of the study area, spectral matching does not. This technology identifies minerals according to the similarity between the target and reference spectra (Meer and Bakker, 1997). It does not need training samples and thresholds to be selected. Thus, spectral matching technology can be used to realize fast and automatic mineral mapping. However, the spectral identification of minerals requires hyperspectral sensors with a high signal-to-noise ratio. In other words, noise may cause spectral matching technology to miss some mineral types.

Clustering (i.e., unsupervised classification) is a common method used to identify objects in hyperspectral images (Xu et al., 2017; Dong et al., 2016). Clustering is a basic problem that arises in many different areas, such as data mining, machine learning, pattern recognition, and image classification (Xu and Wunsch, 2005; Filippone et al., 2008). The aim is to group similar data points into the same cluster, and there is also no need to select training samples.

In fact, clustering and spectral matching can complement each other. The clustering results only reflect the distribution of different clusters; they need to be matched with the classes of the study area to obtain the final classification results. On the other hand, the spectral matching results usually cannot be modified once the hyperspectral image, spectral library, and similarity measurement method are selected. The randomness of clustering makes it possible to obtain various clustering results. Thus, various matching results can be obtained by matching these clustering results with a spectral library. Because the mineral distributions of these matching results are not the same, they can be combined to remove the influence of noise on spectral matching. In other words, the randomness of clustering can make up the unicity of spectral matching.

The k-means algorithm is one of the most commonly used and well-studied clustering methods (Macqueen, 1965). The aim of k-means is to divide all data points into cluster centers so that the sum of the intra-cluster variance is minimized (Tzortzis and Likas, 2014). It includes four steps: (1) initialization, where the number of cluster centers (K) is set and the initial cluster centers are randomly selected; (2) division, where the data points are divided into the nearest cluster centers according to the Euclidean distance (ED) between pixels and cluster

centers; (3) updating, where new cluster centers are obtained by calculating the average reflectance value of pixels; and (4) iteration, where the process goes back to step 2 until the cluster centers do not change or the specified iteration number is reached. Despite its speed and simplicity, the traditional k-means algorithm still has some drawbacks. It uses ED to measure the similarity of each data point and cluster centers. However, ED is sensitive to dimensions, so the traditional k-means is only applicable to the case of uniform metrics. Because remote sensing images always have a limited spatial resolution, mixed pixels where the same mineral type has different reflectance values are inevitable, which can definitely affect the clustering results. The indeterminacy of K also poses a challenge to mineral mapping. The clustering results of k-means heavily depend on the initial cluster centers (Peña et al., 1999; Likas et al., 2003); different initial cluster centers may lead to different clustering results.

To address these problems, an improved k-means algorithm (CKM) was developed in this study. It replaces ED with a dimensionless similarity measurement methods. The spectral absorption features of minerals are enhanced to weaken the influence of mixed pixels on clustering. Combined spectral matching (CSM) is used to match the cluster centers with the United States Geological Survey (USGS) spectral library to obtain the mineral mapping results. CSM takes the mode of various matching results as the final mineral type. Then, K is initialized to 1, and different mapping results are combined with increasing K . During clustering, the initial cluster centers are fixed in the range of $(u - \sigma, u + \sigma)$ according to the three-sigma criteria.

3. Study area and data

3.1. Study area

Cuprite is a famous hydrothermal alteration area in Nevada, USA, with various mineral types and little vegetation (Abrams et al., 1977) and was selected as the study area (Fig. 1(a)). Cuprite has long been used as a test site by many researchers (Hook et al., 1992; Harmer et al., 2009), so the results can be compared to those of a wide range of studies. In particular, Clark and Swayze (Swayze et al., 1992; Clark and Swayze, 1995) generated a mineral distribution map (Fig. 1(c)) of Cuprite (Clark, 2003; Swayze et al., 2003; Swayze et al., 2014) by analyzing the vibrational absorption features of minerals. Fig. 1(c) is derived from USGS. Cuprite mainly has six minerals distributed in three argillaceous alteration zones: alunite, kaolinite, montmorillonite, muscovite, calcite, and chalcedony (Chen et al., 2007).

3.2. AVIRIS image

Airborne visible/infrared imaging spectrometer (AVIRIS) (Vane et al., 1993) was developed by the National Aeronautics and Space Administration (NASA)/Jet Propulsion Laboratory (JPL) and can cover a spectral range of 0.37–2.5 μm with a spectral resolution of 10 nm and 224 contiguous bands in total. In this study, the AVIRIS image came from Environment for Visualizing Images (ENVI) and had 50 shortwave infrared bands covering a wavelength range of 1.99–2.48 μm with a spatial resolution of 20 m. This image was chosen because AVIRIS images after atmospheric correction often have two obvious water vapor absorption bands near 1.45 and 1.95 μm (Kruse et al., 2002; Kruse, 2004). Thus, only the shortwave infrared bands of 2.0–2.5 μm can be used for mineral mapping. This image was processed by an empirical flat field optimized reflectance transformation to remove residual saw-tooth instrument noise and atmospheric effects from calibrated data (Gao and Goetz, 1990; Boardman, 1998). In addition, geometric registration was performed on the mineral distribution map to assess the accuracy. The root mean square error of the registration was less than 1 pixel. Fig. 1(b) shows the three-dimensional cube of the AVIRIS image. More bands in the hyperspectral image mean a thicker cube. The first layer is a false color image composed of the 176th,

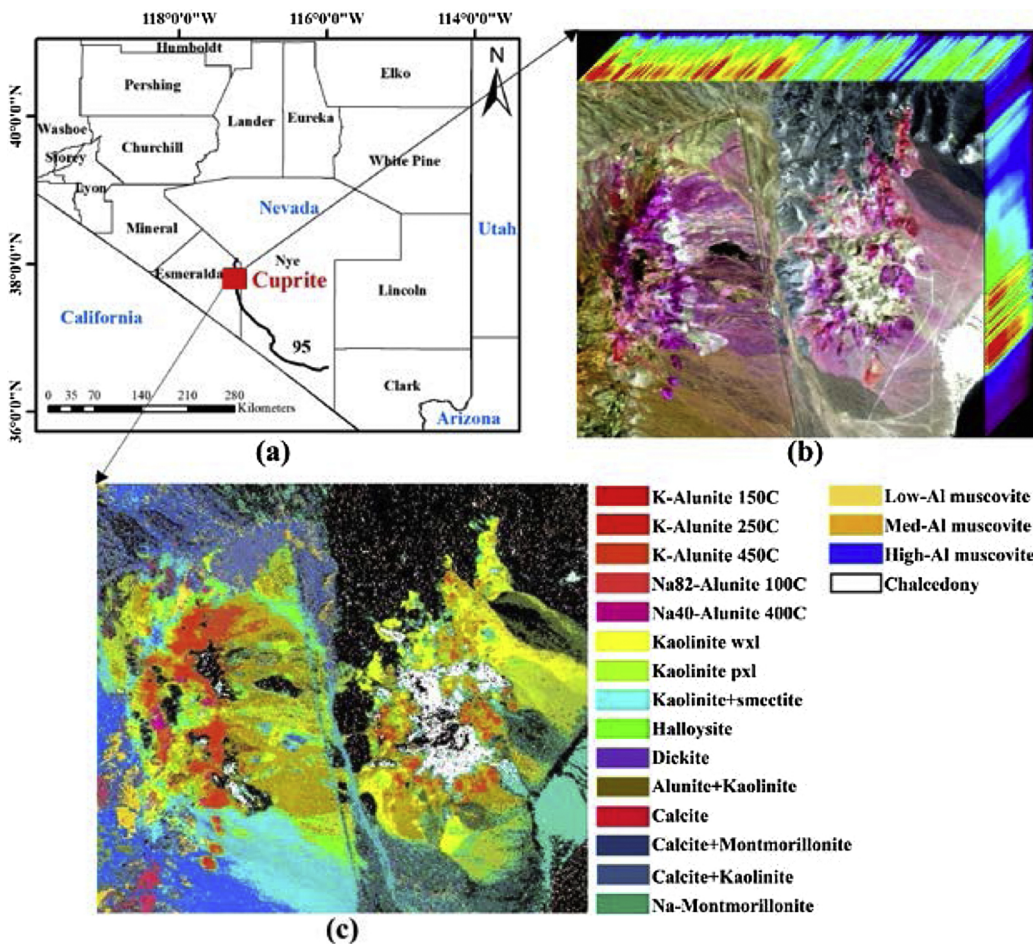


Fig. 1. Study area and data: (a) location map, (b) AVIRIS image, and (c) mineral distribution map from USGS.

190th, and 209th bands, which were selected according to the optimum index factor (OIF) (Chavez et al., 1982). The OIF value is based on the variances and correlation coefficients of any three bands. The band combination with the largest OIF is used for color compositing because it has the most information with the minimal redundancy. A comparison with the mineral distribution map showed that the different colors of the first layer image indicate the distribution of various mineral types.

3.3. Spectral library

Since the clustering results of k-means only reflect the distribution of minerals without giving specific mineral types, the clustering results need to be matched with a spectral library, which is a collection of reflectance data of various objects measured by a spectrometer. Spectral library plays an important role for quick and accurate object identification. The USGS spectral library has more mineral types than other spectral libraries with 481 mineral spectral curves obtained by a Beckman UV-5270 spectrometer at the Denver Spectroscopy Lab (Clark et al., 1993). Thus, it was selected for spectral matching. Each spectral curve of the USGS spectral library has 420 bands covering a spectral range of 0.4–2.5 μm . The wavelength accuracy is about 0.5 nm in the near-infrared range and 0.2 nm in the visible range. As shown in Fig. 2, although the spectral absorption features of the Cuprite minerals were mainly distributed in the spectral range of 1.4–2.5 μm , their spectral curve shapes and diagnostic spectral features differed, which is a prerequisite for hyperspectral mineral mapping.

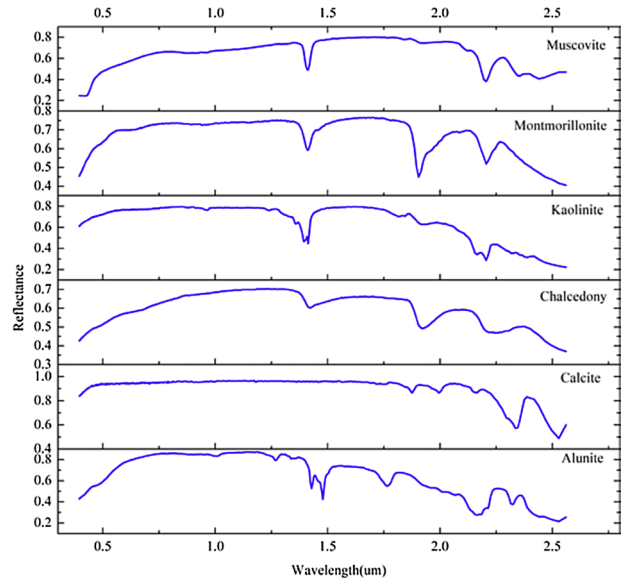


Fig. 2. Spectral curves of Cuprite minerals in the USGS spectral library.

4. Methodology

4.1. Spectral preprocessing

Because the USGS spectral library has a higher spectral resolution than the AVIRIS image, the spectral library needed to be resampled

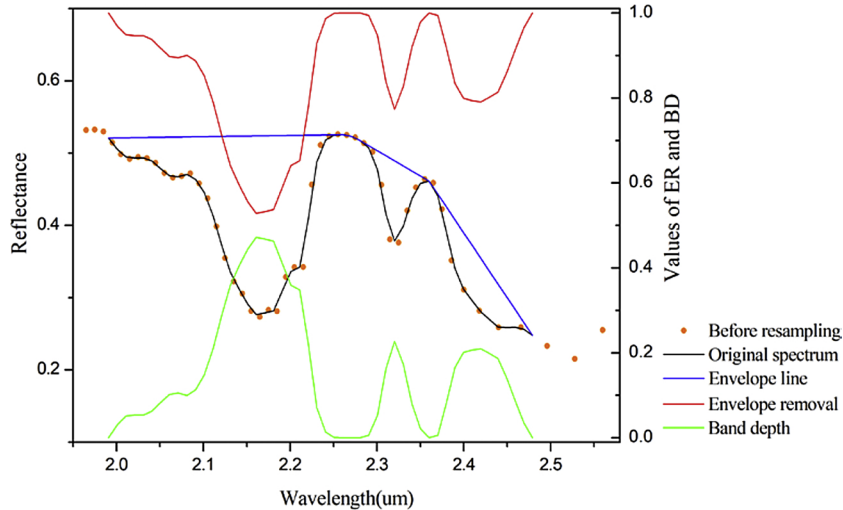


Fig. 3. Spectral curves of alunite before and after preprocessing.

before spectral matching. The wavelength and full width at half maximum of the AVIRIS image were used for resampling with ENVI. In Fig. 3, the orange circles and black line indicate the original spectral curves of alunite before and after resampling, respectively.

After spectral resampling, the spectral differences between various minerals needed to be magnified to enhance their separability. Envelope removal (ER), which is also known as continuum removal, is a spectral processing method that can effectively highlight the spectral absorption features of minerals. The envelope is formed by connecting the extreme points on the spectral curve with segmented straight lines. It looks like a convex hull covering the spectral curve. Then, the envelope is removed by dividing the original spectrum (OS) by the convex hull (Clark and Roush, 1984; Green and Craig, 1985). While enhancing the spectral absorption features, ER can also normalize the reflectivity value to [0, 1]:

$$R_{ci} = \frac{R_i}{R_s + L \cdot (\lambda_i - \lambda_s)} \quad (1)$$

$$L = \frac{R_e - R_s}{\lambda_e - \lambda_s} \quad (2)$$

where R represents the reflectance value, λ is the wavelength; s and e are the starting and ending points of the segmented straight lines of the envelope, respectively; L is the slope of s and e ; and i is the band number. Another spectral enhancement method that was used is the band depth (BD), which is calculated by subtracting ER from 1 (Kokaly and Clark, 1999). BD is associated with the mineral abundance; a deep absorption implies greater abundance. Fig. 3 shows that the envelope completely covered the whole spectral curve, and ER clearly had a greater absorption depth than OS. Meanwhile, BD and ER were exactly symmetric.

4.2. Improved k-means algorithm

To address the drawbacks of the traditional k-means algorithm for mineral mapping, CKM provides three improvements: a modified similarity measurement method, enhanced spectral absorption features, and combined mineral mapping results as K is incremented. Fig. 4 shows a flowchart for the CKM procedure. To address the drawbacks of ED, the spectral angle mapper (SAM) (Kruse et al., 1993a) and spectral correlation coefficient (SCC) were used for similarity measurement of clusters because they are insensitive to dimensions. SAM measures the similarity of data points and cluster centers by calculating the angle between them:

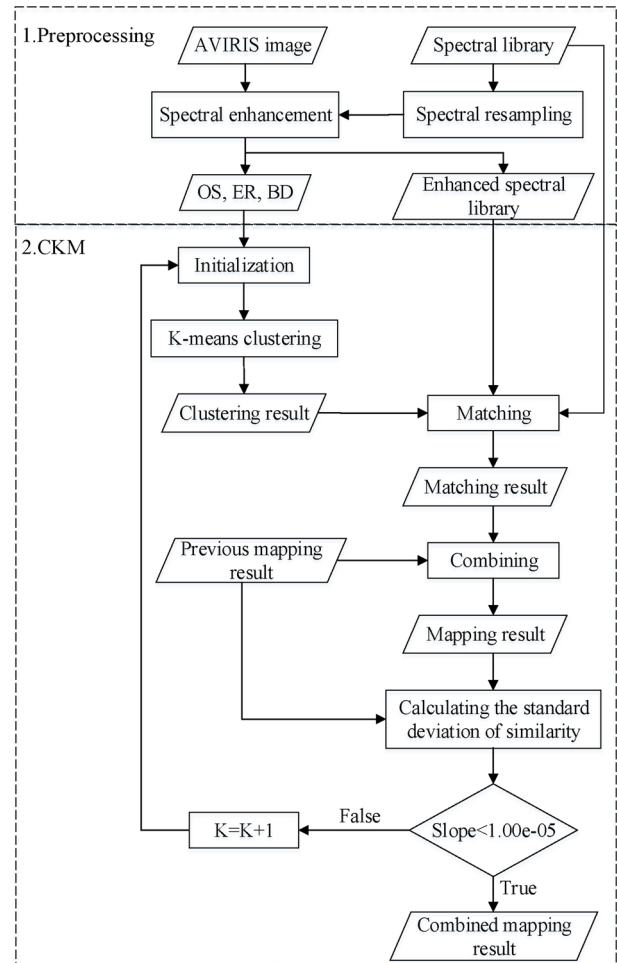


Fig. 4. Flowchart for the CKM procedure.

$$\cos \alpha = \frac{A \cdot B}{\|A\| \cdot \|B\|} = \frac{\sum_{i=1}^n A_i B_i}{(\sqrt{\sum_{i=1}^n A_i^2})(\sqrt{\sum_{i=1}^n B_i^2})} \quad (3)$$

where A and B represent the spectral vectors of data points and cluster centers, respectively, and n is the number of bands. Compared with ED, SAM focuses on the spectral shape difference rather than the numerical difference. The cosine of the spectral angle is between 0 and 1. A

smaller spectral angle indicates greater similarity between A and B . SCC uses a Pearson correlation coefficient to measure the similarity:

$$R_{AB} = \frac{\sigma_{AB}^2}{\sigma_{AA}\sigma_{BB}} = \frac{\sum_{i=1}^n (A_i - \bar{A})(B_i - \bar{B})}{\sqrt{\sum_{i=1}^n (A_i - \bar{A})^2} \sqrt{\sum_{i=1}^n (B_i - \bar{B})^2}} \quad (4)$$

where σ_{AB}^2 is the covariance and σ_{AA} and σ_{BB} are standard deviations. The range of the correlation coefficient is [-1, 1]. In contrast to SAM, a larger correlation coefficient indicates a greater similarity between A and B . In fact, a comparison of Eqs. (4) and (5) shows that both SCC and SAM measure the similarity of two vectors by calculating the cosine angle between them. The three similarity measurement methods (ED, SAM, and SCC) and three spectral features (OS, ER, and BD) were used to develop nine classifiers: OS-ED, OS-SAM, OS-SCC, ER-ED, ER-SAM, ER-SCC, BD-ED, BD-SAM, and BD-SCC. Because the clustering result of k-means varies with the initial cluster centers, the initial cluster centers were fixed to the range of $(u - \sigma, u + \sigma)$ so that the mineral mapping results of different classifiers could be compared according to the three-sigma criteria:

$$C_i = (u - \sigma) + \frac{i * (2 * \sigma)}{K}, \quad i = 1, \dots, K \quad (5)$$

where u is the mean value, σ is the standard deviation, and C_i is the i th cluster center.

After clustering, CSM was used to match the spectra of cluster centers with the USGS spectral library for the mineral mapping results because a single spectral matching method may miss some mineral types. CSM includes three steps: (1) ED, SAM and SCC are used to match the cluster centers with the USGS spectral library; (2) Take the minerals of Cuprite in each matching result; and (3) The mode of these minerals is used as the mineral type of the cluster center. If there are multiple modes, the mode with the greatest similarity is taken as the final mineral type.

K is initialized to 1. Then, the matching result and previous mineral mapping result (PMMR) are combined pixel by pixel as K is incremented. Thus, the value of K does not need to be specified in advance. The principle of combination is that the matching result only replaces PMMR when it contains new minerals of Cuprite. Otherwise, PMMR is taken as the current mineral mapping result (CMMR). The similarity between PMMR and CMMR is used as the condition for iteration termination:

$$S = \frac{N * 1.0}{nl * ns} \quad (6)$$

where S is the similarity, N is the number of pixels with a value of 0 in the difference image between PMMR and CMMR, and nl and ns are the numbers of rows and columns, respectively. The similarity can be used to measure the consistency of the mineral type and quantity between PMMR and CMMR. Theoretically, when the standard deviation is 0, the similarity is stable. However, the randomness of clustering results means that the standard deviation of similarity can only be infinitely close to 0. Therefore, in order to keep K sufficiently large and avoid outliers, the similarity is considered to be stable and the iteration stops when 20 adjacent standard deviation slopes are less than 1.00e-05. Then, CMMR is taken as the combined mineral mapping result. Otherwise, K is incremented by 1, and CKM continues to carry out the next clustering.

4.3. Accuracy assessment

The performance of each classifier was evaluated in two ways: the clustering accuracy and mapping accuracy. The clustering performance can be validated in two ways: external and internal indices. The former needs the true values, while the latter does not. In this study, the Davies–Bouldin index (DBI) (Liu et al., 2010) was used to evaluate the clustering accuracy, while the overall accuracy (OA) and kappa

coefficient (KC) (Congalton, 1991) were used to evaluate the mapping accuracy.

DBI is an internal clustering index, and its basic concept is that the inter-cluster separation should have high homogeneity and compactness (Davies and Bouldin, 1979). DBI combines two measures: the dispersion and clustering similarity.

$$DBI = \frac{1}{K} \sum_{i=1}^k \max \left(\frac{\text{avg}(C_i) + \text{avg}(C_j)}{d(C_i, C_j)} \right) \quad (7)$$

Here, $\text{avg}(C_i)$ and $\text{avg}(C_j)$ are the sample mean values of the i th and j th clusters, respectively, and $d(C_i, C_j)$ is the distance between C_i and C_j . A smaller DBI indicates better clustering results. However, DBI can only be used to evaluate the clustering accuracy when different classifiers have the same K values.

OA is the probability that the classification results are consistent with the actual results. It only considers the number of pixels correctly classified in the diagonal direction, while KC considers all kinds of missing and wrong pixels outside the diagonal direction. Therefore, KC is usually less than OA.

$$OA = \frac{n}{\sum_{i=1}^n x_{ii}} / N \quad (8)$$

$$KC = \frac{N \sum_{i=1}^n x_{ii} - \sum_{i=1}^n (x_{i+} + x_{+i})}{N^2 - \sum_{i=1}^n (x_{i+} + x_{+i})} \quad (9)$$

Here, n is the number of mineral types, x_{ii} is the sum of the confusion matrix diagonals, N is the total number of samples, x_{i+} is the sum of the i th predicted mineral, and x_{+i} is the sum of the i th mineral in the sample.

5. Results

Fig. 5 shows the clustering results for SKM (i.e., the k-means when $K = 6$). The comparison with the mineral distribution map shows that only the clustering result with OS-ED was disordered, while the other clustering results reflected the mineral distribution well. To evaluate the clustering accuracy, the mineral distribution map and clustering results were used as input data for DBI. Table 1 indicates that OS-ED had a larger DBI than the other classifiers, which means that it had the worst clustering accuracy. This is consistent with the results of the qualitative analysis. OS-SAM and OS-SCC had much lower DBI values than OS-ED. Thus, SAM and SCC provided better clustering than ED for the original hyperspectral image. For ER, ED and SAM had similar DBI values that were both less than that of SCC. For BD, ED performed better than SAM and SCC. ER-ED and BD-ED had much lower DBI values than OS-ED, which means that ED can produce better clustering results after spectral enhancement. In terms of the average DBI value, ER and BD outperformed OS, and SAM and SCC outperformed ED.

After clustering, the cluster centers of different spectral features were matched with the USGS spectral library. The mineral mapping results and accuracies of SKM are given in Fig. 6 and Table 2, respectively. Qualitatively, only the OS-ED classifier did not find any mineral. Although OS-SAM and OS-SCC identified alunite, they both misidentified some muscovite as montmorillonite. OS-SAM also identified some kaolinite. The three mapping results of ER only contained alunite. All BD-based classifiers identified alunite and muscovite. With ER or BD, the three similarity measurement methods obtained similar mineral mapping results. Quantitatively, OS-ED had a mapping accuracy of 0. The average OA and KC of OS-SAM and OS-SCC were about 36% and 26% higher, respectively, than those of OS-ED. With ER or BD, each similarity measurement method showed similar performance. In terms of the average mapping accuracy, SAM and SCC performed better than ED, and BD outperformed OS and ER. Because SKM identified few mineral types, the average kappa value was only about 0.22.

The clustering and mapping results of the k-means algorithm

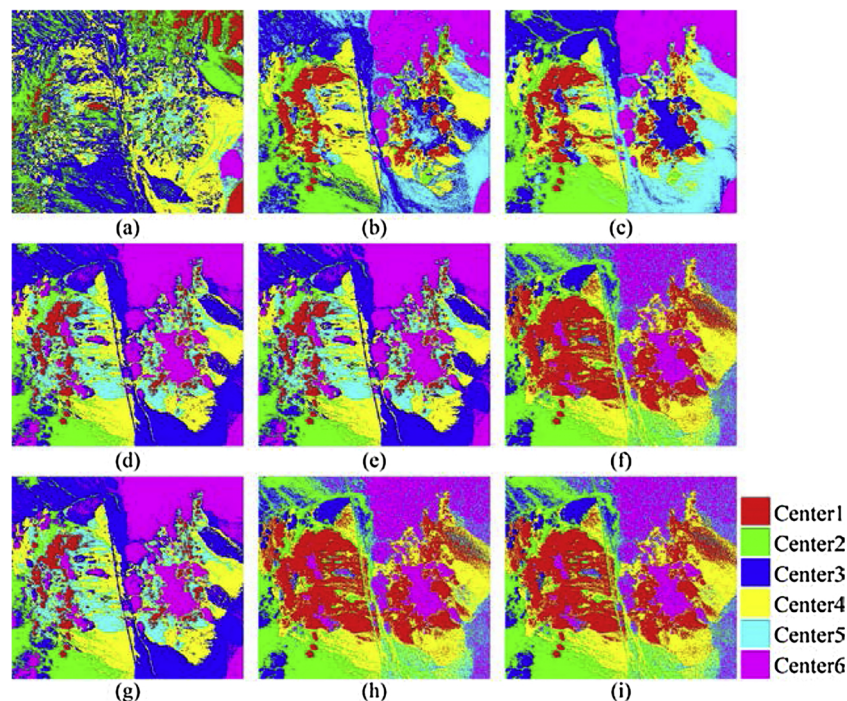


Fig. 5. Clustering results for SKM: (a) OS-ED, (b) OS-SAM, (c) OS-SCC, (d) ER-ED, (e) ER-SAM, (f) ER-SCC, (g) BD-ED, (h) BD-SAM, and (i) BD-SCC.

Table 1
Clustering accuracies for SKM accuracies, 2020
Clustering accuracies for SKM

DBI	OS	ER	BD	Average
ED	8.7664	2.5063	2.5057	4.5928
SAM	2.9827	2.4884	4.9206	3.4639
SCC	2.6385	4.8688	4.8747	4.1274
Average	4.7959	3.2879	4.1004	4.0614

changes with K when the initial clustering center is fixed. Therefore, the similarity between different mineral mapping results was used as the condition for iteration termination in this study. Fig. 7 shows that

the standard deviation of the similarity gradually decreased with increasing K for all classifiers. When $K > 700$, the standard deviation curves tended to be stable, and all of the standard deviations were very close to 0. This indicates that the mineral mapping results of all classifiers hardly changed when K was sufficiently large.

Fig. 8 and Table 2 present the mineral mapping results and accuracies, respectively, for EKM (i.e., the k-means when the iteration ends). Qualitatively, although the three OS-based classifiers identified alunite and kaolinite, they all misidentified some muscovite as montmorillonite. The ER and BD classifiers identified four mineral types: alunite, kaolinite, muscovite, and calcite. Whether ED, SAM, or SCC was used for clustering, the three mineral mapping results of each

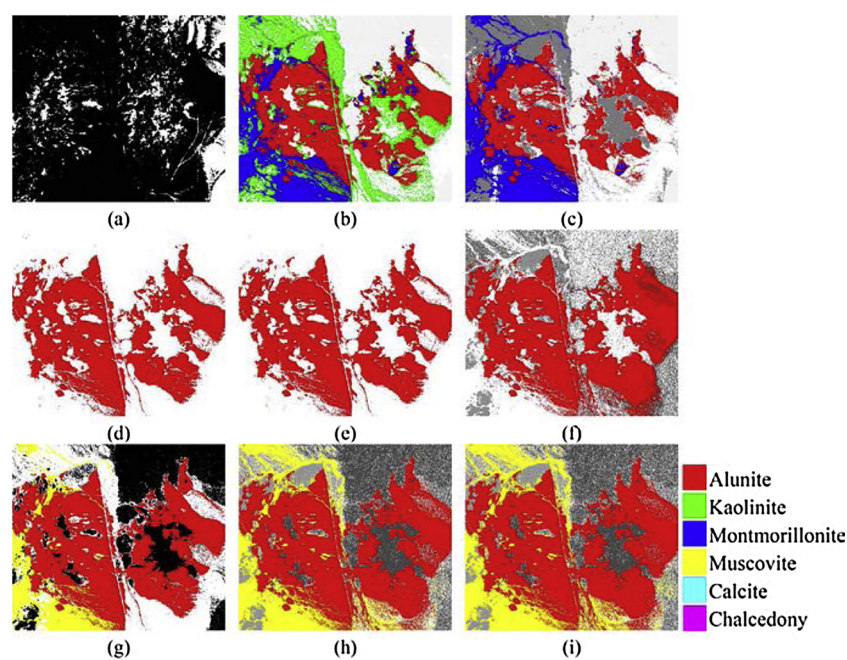
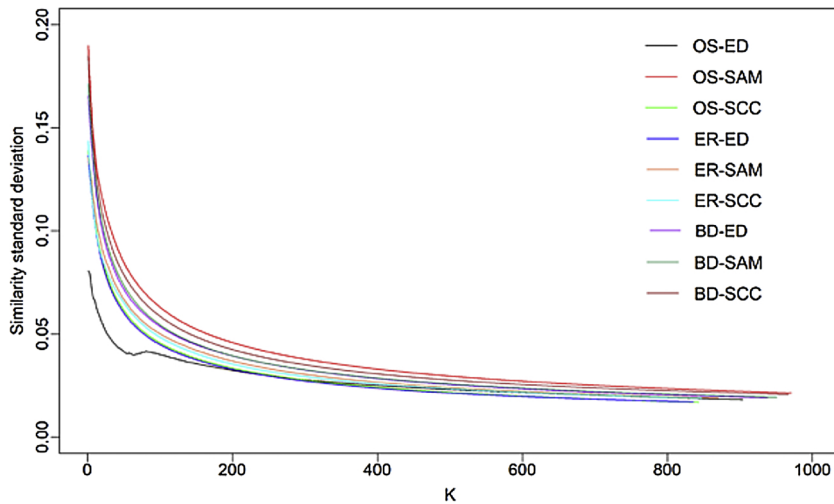


Fig. 6. Mineral mapping results for SKM: (a) OS-ED, (b) OS-SAM, (c) OS-SCC, (d) ER-ED, (e) ER-SAM, (f) ER-SCC, (g) BD-ED, (h) BD-SAM, and (i) BD-SCC.

Table 2

Mineral mapping accuracies of different mapping methods.

Mapping Methods		OA				KC			
		OS	ER	BD	Average	OS	ER	BD	Average
SKM	ED	0.0000	0.2676	0.4149	0.2275	0.0000	0.1611	0.3076	0.1562
	SAM	0.3607	0.2687	0.4372	0.3555	0.2622	0.1637	0.3184	0.2481
	SCC	0.3497	0.2772	0.4361	0.3543	0.2559	0.1692	0.3162	0.2471
	Average	0.2368	0.2711	0.4294	0.3124	0.1727	0.1647	0.3141	0.2172
EKM	ED	0.4886	0.5927	0.5970	0.5594	0.4247	0.5379	0.5418	0.5015
	SAM	0.5106	0.6032	0.6215	0.5784	0.4478	0.5476	0.5697	0.5217
	SCC	0.5275	0.6012	0.6113	0.5800	0.4654	0.5464	0.5583	0.5234
	Average	0.5089	0.5990	0.6099	0.5726	0.4460	0.5440	0.5566	0.5155
Filtered EKM	ED	0.5130	0.6876	0.6562	0.6189	0.4598	0.6434	0.6091	0.5708
	SAM	0.5416	0.6733	0.6664	0.6271	0.4706	0.6322	0.6208	0.5745
	SCC	0.5524	0.6638	0.6681	0.6281	0.4891	0.6185	0.6231	0.5769
	Average	0.5357	0.6749	0.6636	0.6247	0.4731	0.6313	0.6177	0.5741
CSM	Unfiltered	0.4970	0.6224	0.6139	0.5778	0.4368	0.5717	0.5616	0.5234
	Filtered	0.5377	0.5970	0.5944	0.5764	0.4772	0.5356	0.5365	0.5164
CKM	ED	0.5487	0.8358	0.8139	0.7328	0.4496	0.8008	0.7614	0.6706
	SAM	0.5588	0.8192	0.8234	0.7338	0.4623	0.7805	0.7859	0.6762
	SCC	0.5368	0.8292	0.8062	0.7241	0.4659	0.7931	0.7586	0.6725
	Average	0.5481	0.8242	0.8145	0.7302	0.4593	0.7868	0.7686	0.6731

**Fig. 7.** Changes in the curves for the similarity standard deviation.

spectral feature were highly consistent. Quantitatively, **Table 2** indicates that EKM not only identified more mineral types than SKM but also greatly improved the mineral mapping accuracy. The average OA and KC of EKM were about 26% and 30% higher, respectively, than those of SKM. Although OS-ED still had the lowest mapping accuracy among all classifiers for EKM, it performed much better than for SKM. In terms of the average mapping accuracy, ER and BD outperformed OS, while the similarity measurement methods showed similar performances.

Fig. 9 and **Table 2** present the combined mineral mapping results and accuracies of CKM, respectively. Qualitatively, the mineral mapping results of CKM showed little difference for the same spectral feature regardless of the similarity measurement method. The OS-based classifiers identified alunite and kaolinite. Like EKM, the three OS-based classifiers misidentified some muscovite as montmorillonite. All ER- and BD-based classifiers identified alunite, kaolinite, muscovite, and calcite. The three ER-based classifiers identified a little chalcedony, and the ER-ED classifier also identified Na-Montmorillonite. Quantitatively, the average OA and KC of CKM were about 42% and 46% higher, respectively, than those of SKM, and 16% higher than those of EKM. Each similarity measurement method showed a similar average mapping accuracy. The average OA and KC after spectral enhancement were about 27% and 32% higher than OS.

6. Discussion

In terms of the clustering and mapping accuracies of SKM, SAM and SCC outperformed ED for OS, while ER and BD outperformed OS for ED. This suggests that the clustering and mapping results of traditional k-means can be improved by using dimensionless similarity measurement methods or enhancing spectral absorption features. Meanwhile, for the original spectrum, SKM with SAM outperformed SKM with SCC. For EKM and CKM, the mineral mapping results of OS-SAM and OS-SCC are close. No matter which mapping method was used, SAM and SCC based on ER and BD have similar performance in mineral mapping. Moreover, SKM with BD outperformed SKM with ER. For EKM and CKM, the mineral mapping results of ER and BD have little difference. In addition, CKM performed better than SKM and EKM, which indicates that the mineral mapping accuracy can be improved by combining different mineral mapping results.

The clustering and mapping results of SKM indicated that there are always more cluster centers than identified mineral types. This may be because some cluster centers are mismatched, or some cluster centers are identified as the same mineral type. For example, SKM identified both Centers 1 and 4 in **Fig. 10** as alunite. However, according to the mineral distribution map, Center 4 is actually a mixed pixel that includes alunite and kaolinite. Thus, SKM missed kaolinite, while EKM

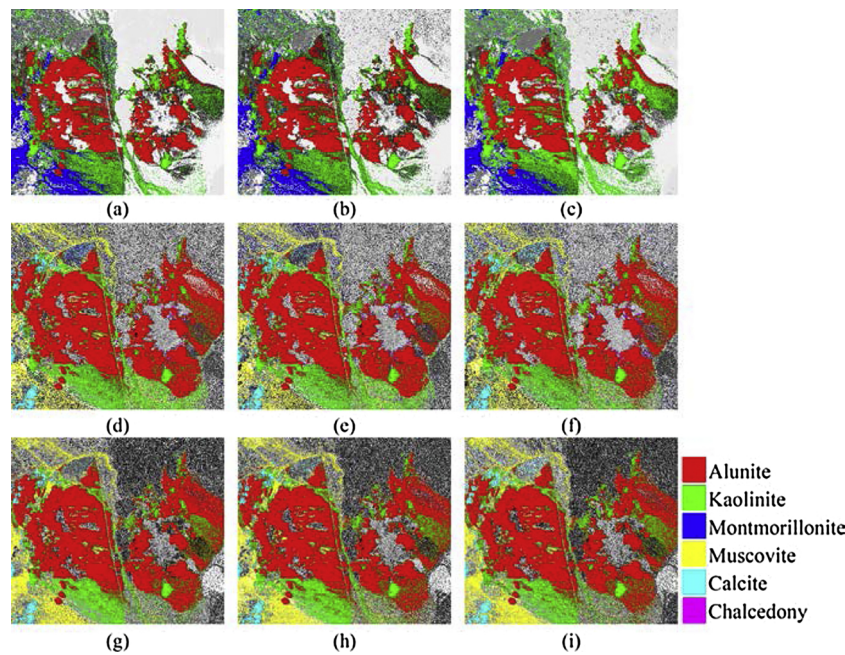


Fig. 8. Mineral mapping results for EKM: (a) OS-ED, (b) OS-SAM, (c) OS-SCC, (d) ER-ED, (e) ER-SAM, (f) ER-SCC, (g) BD-ED, (h) BD-SAM, and (i) BD-SCC.

and CKM identified both minerals. Except for OS-SAM, the other classifiers of EKM and CKM identified more mineral types than SKM. This suggests that setting K greater than the number of mineral types will help with finding more mineral types.

The difference between CKM and traditional spectral matching is that the latter matches each pixel of the hyperspectral image with the spectral library, while the former matches each cluster center. In order to compare their performance in mineral mapping, CSM was used to match the AVIRIS image with the USGS spectral library pixel by pixel. Fig. 11(1) and Table 2 indicate that the mineral mapping results and accuracies of CSM were basically consistent with those of EKM. In other words, CKM is more effective at mineral mapping than traditional spectral matching.

The mineral mapping results in Figs. 8 and 11(1) are generally

fragmentary. This is because the noise of the AVIRIS image makes the spectral curve not smooth. To address this problem, the Hamming window filter (HWF) (Megat Ali et al., 2014) was used for low-pass filtering of the AVIRIS image:

$$w(i) = 0.54 - 0.46 * \cos\left(2\pi * \frac{i}{n-1}\right), i = 1, \dots, n \quad (10)$$

where $w(i)$ is the Hamming window coefficient and n is the length of HWF and was set to 3. Fig. 12 shows the original spectral curve of a pixel in the AVIRIS image before and after filtering. Although the filtered spectrum shifted slightly upward, the spectral curve is much smoother than before, and its shape is basically unchanged. Fig. 11(2) and Table 2 indicate that the filtered mineral mapping results of CSM were much smoother than those without filtering, and the mapping

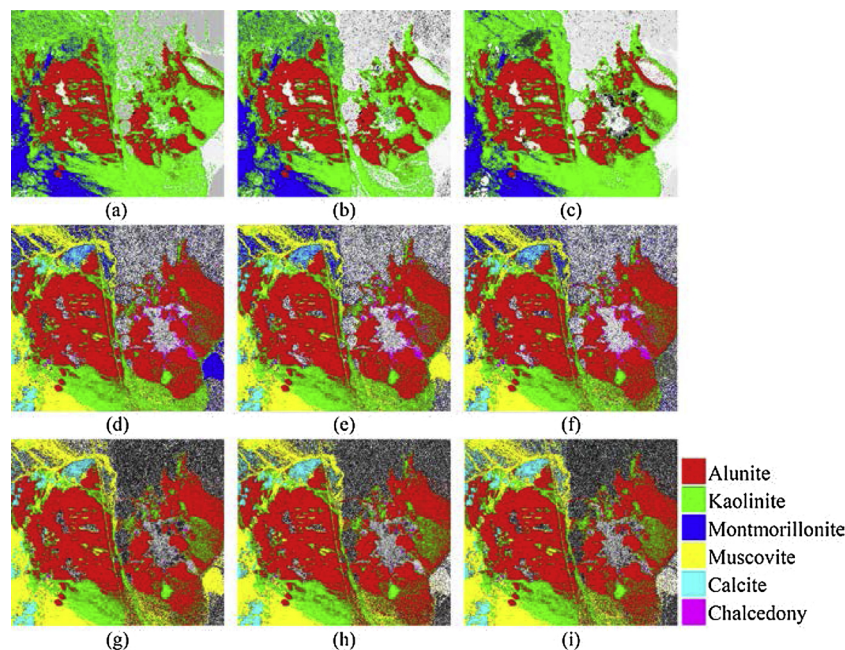


Fig. 9. Mineral mapping results for CKM: (a) OS-ED, (b) OS-SAM, (c) OS-SCC, (d) ER-ED, (e) ER-SAM, (f) ER-SCC, (g) BD-ED, (h) BD-SAM, and (i) BD-SCC.

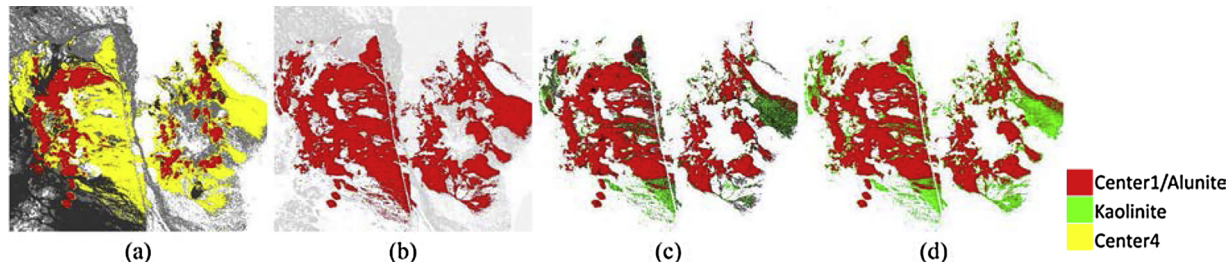


Fig. 10. Comparison between the clustering and mapping results with the OS-SAM classifier: (a) clustering results; mapping results with (b) SKM, (c) EKM, and (d) CKM.

accuracy was improved with OS. For ER and BD, however, most muscovite pixels were lost after filtering, which makes the mapping results worse than that without filtering. This is because when ER and BD were used to enhance spectral absorption features, the noise signal in the spectrum of each pixel will also be amplified.

To address this problem, EKM was used for clustering with the filtered image, while the cluster centers with the unfiltered spectra were matched with the USGS spectral library. This not only smoothed the burrs of the spectral curves but also kept the original spectral features. A comparison between Figs. 8 and 13 shows that, while the mineral mapping results were smoothed, the types and distribution of minerals basically remained unchanged. In terms of the mapping accuracy, the filtered EKM performed better than that without filtering and CSM. This suggests that, compared with traditional spectral matching, the improved k-means method can make full use of HWF to improve the mineral mapping results of ER and BD.

Although CKM basically identified the same mineral types as EKM, the mineral distributions of the former were more contiguous and extensive. Meanwhile, the average OA and KC of CKM were about 11% and 10% higher, respectively, than those of the filtered EKM. This is because the randomness of the clustering caused different mineral distributions with the various mapping results, which means that a pixel that was misidentified for one mapping result because of noise may be correctly identified for another. That is to say, different mineral mapping results can complement each other. Therefore, CKM can reduce speckle noise in the mapping results to some extent and performs better than filtered EKM in mineral mapping.

Fig. 14 shows the similarities between the mineral mapping results of ED with SAM and ED with SCC, which were also calculated according to equation (6). For OS, the mineral mapping results of ED were increasingly similar to those of SAM and SCC with increasing. For ER and BD, the similarities between the mineral mapping results of ED with

SAM and ED with SCC remained high. When $K > 600$, all similarity curves tend to be stable. This indicates that the k-means mineral mapping results with OS were hardly affected by the similarity measurement method when K was much greater than the number of mineral types. For ER and BD, the mineral mapping results were strongly consistent regardless of K and the similarity measurement method. Thus, the k-means mineral mapping results for any spectral feature were independent of dimensional differences when K was sufficiently large. This is because the k-means algorithm updates the cluster center by calculating the average reflectance of all pixels in the cluster, so the mineral mapping results improve with the probability that all pixels of each cluster belong to the same mineral type. A larger K means that each cluster contains fewer pixels, which increases the probability that these pixels belong to the same mineral type. Meanwhile, regardless of, the pixels of each cluster are likely to belong to the same mineral type as long as the clustering results accurately reflect the distributions of various minerals.

The mineral mapping methods used in this paper classify each pixel into one mineral without considering the processing of mixing problem. At present, in addition to spectral unmixing, other remote sensing classification methods usually classify each mixed pixel into one feature, because there is always a feature that plays a leading role in the mixed spectrum. The processing of mixing problem usually includes the determination of mineral types and the calculation of mineral proportions. Spectral matching can get the similarities between each pixel and various minerals. Meanwhile, the similarities of these minerals are related to their contents in mixed pixel. The higher the content, the greater the similarity. Therefore, to address the mixing problem, the matching similarity can be used to calculate the proportion of various minerals of each pixel in the next work.

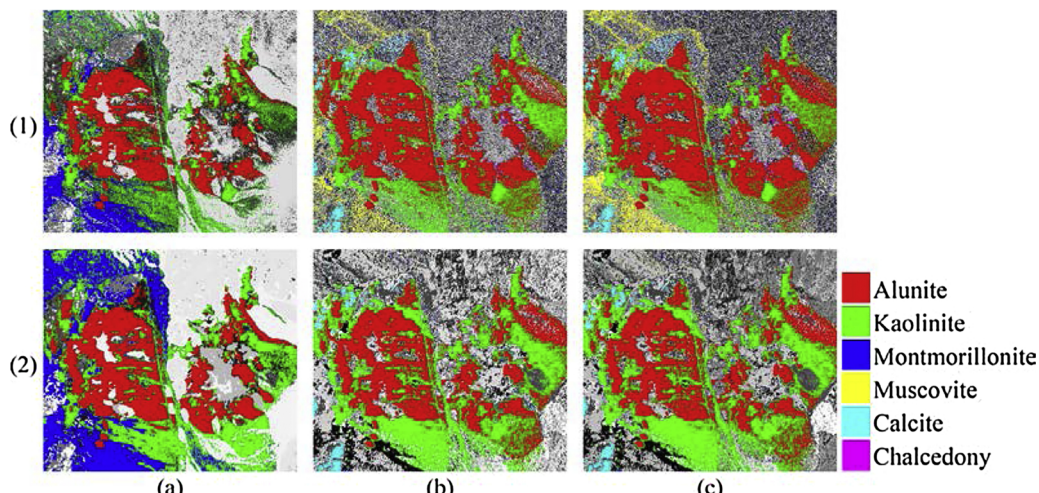


Fig. 11. Mineral mapping results of CSM (1) before and (2) after filtering: based on (a) OS, (b) ER and (c) BD.

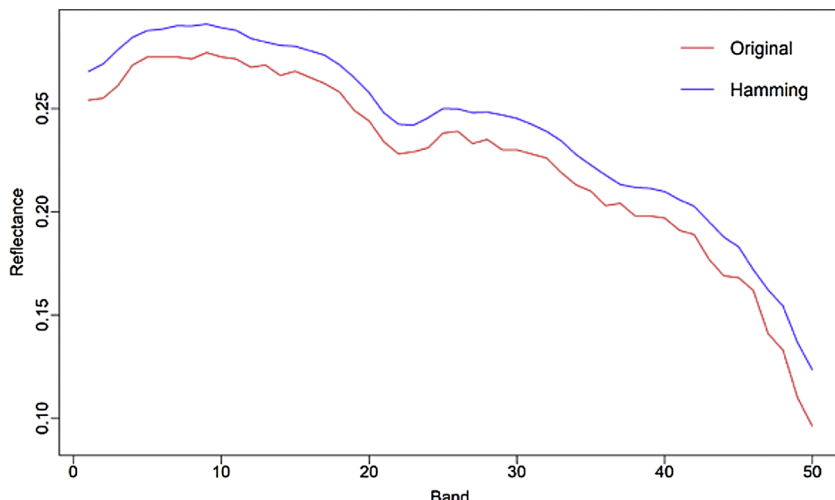


Fig. 12. Original spectral curves before and after filtering.

7. Conclusions

To address the drawbacks of traditional k-means and spectral matching on mineral mapping, an improved k-means algorithm was developed. CKM uses SAM and SCC instead of ED and combines the mineral mapping results with increasing. ER and BD are used to enhance the spectral absorption features. Experiments showed that CKM is more effective at mineral mapping than traditional k-means and spectral matching. The clustering and mapping accuracies of k-means can be improved by using a dimensionless similarity measurement method or enhancing the spectral absorption features. The mineral mapping results can be improved by setting K sufficiently large because a larger K is conducive to find new mineral types. CKM uses the

randomness of k-means to make up for the unicity of spectral matching technology and effectively removes the speckle noise in the mineral mapping results. When K is sufficiently large, the k-means mapping results are hardly affected by the similarity measurement method. However, the proposed method requires high accuracy for atmospheric correction and a complete spectral library as support, which may limit its applicability.

8. Declaration of interests

The authors declare that they have no known competing financial interests or personal relationships that could have appeared to influence the work reported in this paper.

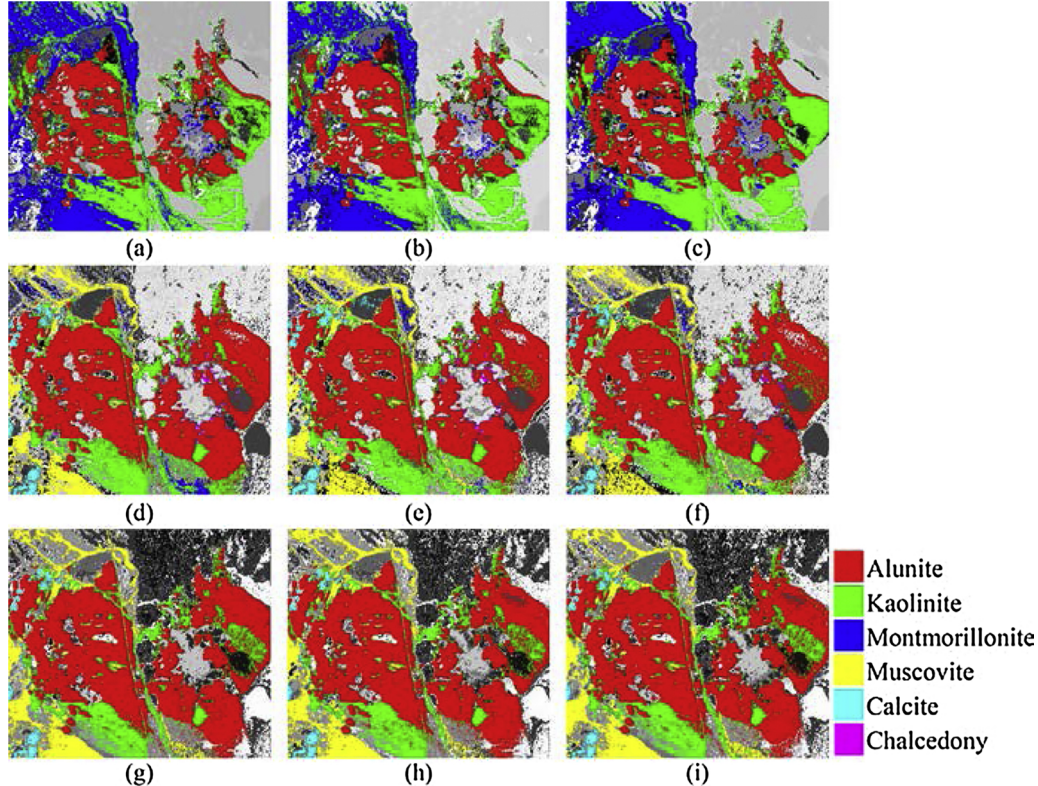


Fig. 13. Mineral mapping results with EKM after filtering: (a) OS-ED, (b) OS-SAM, (c) OS-SCC, (d) ER-ED, (e) ER-SAM, (f) ER-SCC, (g) BD-ED, (h) BD-SAM, and (i) BD-SCC.

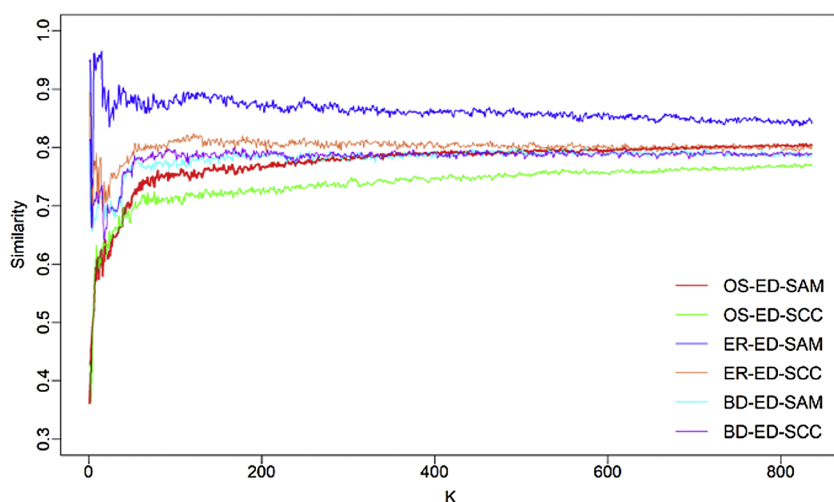


Fig. 14. Similarity curves for the mineral mapping results of ED with SAM and ED with SCC. OS-ED-SAM represents the similarity of mineral mapping results of OS-ED and OS-SAM and so on.

9. Authorship contributions

Zhongliang Ren: Methodology, Software, Validation, Investigation, Visualization, Writing original draft.

Lin Sun: Conceptualization, Reviewing, Supervision and Funding acquisition.

Qiuping Zhai: Software, Reviewing and editing, Supervision.

Acknowledgments

The authors would like to thank Dr. Qiuping Zhai for helping improve the quality of the manuscript. Funding: This work was supported by the National Natural Science Foundation of China [grant number No.41771408]; and the Shandong Provincial Natural Science Foundation [grant number No. ZR201702210379].

References

- Abedi, M., Norouzi, G.H., Bahroudi, A., 2011. Support vector machine for multi-classification of mineral prospectivity areas. *Comput. Geosci.* 9, 272–283.
- Abrams, M.J., Ashley, R.P., Rowan, L.C., Goetz, A.F.H., Kahle, A.B., 1977. Mapping of hydrothermal alteration in the Cuprite mining district, Nevada using aircraft scanner images for the spectral region 0.46–2.36 μm. *Geology* 5, 713–718.
- Abubakar, A.J., Hashim, M., Pour, B.A., 2018. Hydrothermal alteration mapping of mineralogical imprints associated with subtle geothermal system using mixture tuned matched filtering approach on ASTER vnr and swir data. *ARPN Journal of Engineering and Applied Sciences*. 13 (4), 1226–1234.
- Bhadra, B.K., Pathak, S., Karunakar, G., Sharma, J.R., 2013. ASTER data analysis for mineral potential mapping around Sawar-Malpura area, Central Rajasthan. *Journal of the Indian Society of Remote Sensing*. 41 (2), 391–404.
- Boardman, J.W., 1998. Post-ATREM polishing of AVIRIS apparent reflectance data using EFFORT: A lesson in accuracy versus precision, in: *Summaries of the Seventh JPL Airborne Earth Science Workshop*. JPL, Pasadena, CA.
- Chavez, P.L., Berlin, G.L., Sowers, L.B., 1982. Statistical Method for Selecting Landsat MSS Ratios. *Journal of Applied Photographic Engineering*. 8 (1), 23–30.
- Chen, X., Warner, T.A., Campagna, D.J., 2007. Integrating visible, near-infrared and short-wave infrared hyperspectral and multispectral thermal imagery for geological mapping at Cuprite, Nevada. *Remote Sens. Environ.* 110 (3), 344–356.
- Clark, R.N., 2003. Imaging spectroscopy: Earth and planetary remote sensing with the USGS Tetracorder and expert systems. *Journal of Geophysical Research*. 108(E12) 5131.
- Clark, R.N., Roush, T.L., 1984. Reflectance spectroscopy: Quantitative analysis techniques for remote sensing applications. *Jour. Geophys. Res.* 89, 6329–6340.
- Clark, R.N., Swayze, G.A., Gallagher, A.J., King, T.V.V., Calvin, W.M., 1993. The U.S. Geological Survey, Digital Spectral Library: Version 1 (0.2 to 3.0 μm). Open File Report 93-592. USGS, Reston, VA.
- Clark, R.N., Swayze, G.A., 1995. Automated spectral analysis: Mapping minerals, amorphous materials, environmental materials, vegetation, water, ice and snow, and other materials: The USGS tricorder algorithm, in: *Proceedings of the Lunar & Planetary Science Conference*. Lunar and Planetary Institute, Houston, TX, pp. 255.
- Congalton, R.G., 1991. A review of assessing the accuracy of classifications of remotely sensed data. *Remote Sens. Environ.* 37, 35–46.
- Craw, D., Upton, P., Mackenzie, D.J., 2009. Hydrothermal alteration styles in ancient and modern orogenic gold deposits, New Zealand. *New Zealand Journal of Geology & Geophysics*. 52 (1), 11–26.
- Davies, D.L., Bouldin, D.W., 1979. A cluster separation measure. *IEEE Trans. Pattern Anal. Mach. Intell.* PAMI-1(2) 224–227.
- Dong, W., Fu, F., Shi, G., Cao, X., Wu, J., Li, G., Li, X., 2016. Hyperspectral image super-resolution via non-negative structured sparse representation. *IEEE Trans. Image Process.* 25 (5), 2337–2351.
- Filippone, M., Camastrà, F., Masulli, F., Rovetta, S., 2008. A survey of kernel and spectral methods for clustering. *Pattern Recognit.* 41 (1), 176–190.
- Fisher, I.S., 1998. Mineral identification, classical field methods. Springer, Boston, MA.
- Gao, B.C., Goetz, A.F.H., 1990. Column atmospheric water vapor and vegetation liquid water retrievals from airborne imaging spectrometer data. *J. Geophys. Res. Atmos.* 95 (D4), 3549–3564.
- Green, A.A., Craig, M.D., 1985. Analysis of aircraft spectrometer data with logarithmic residuals. *Proc. Airborne Imaging Spectrometer Data Analysis Workshop* 111–119.
- Harmer, S.L., Skinner, W.M., Buckley, A.N., Fan, L.-J., 2009. Species formed at cuprite fracture surfaces; observation of O 1s surface core level shift. *Surf. Sci.* 603 (3), 537–545.
- Hook, S.J., Gabell, A.R., Green, A.A., Kealy, P.S., 1992. A comparison of techniques for extracting emissivity information from thermal infrared data for geologic studies. *Remote Sens. Environ.* 42 (2), 123–135.
- Hunt, G.R., 1979. Near-infrared (1.3–2.4 μm) spectra of alteration minerals – potential for use in remote sensing. *Geophysics* 44 (12), 1974–1986.
- Kakroodi, M.G., Huger, M., Gault, C., Chotard, T., 2009. Anisotropic behaviour of analusite particles used as aggregates on refractory castables. *J. Eur. Ceram. Soc.* 29 (4), 571–579.
- Kokaly, R.F., Clark, R.N., 1999. Spectroscopic determination of leaf biochemistry using band-depth analysis of absorption features and stepwise multiple linear regression. *Remote Sens. Environ.* 67 (3), 267–287.
- Kruse, F.A., 2004. Comparison of ATREM, ACORN, and FLAASH atmospheric corrections using low-altitude AVIRIS data of Boulder, CO, in: *Proc. 13th JPL Airborne Geoscience Workshop*. JPL, Pasadena, CA.
- Kruse, F.A., Lefkoff, A.B., Boardman, J.W., Heidebrecht, K.B., Shapiro, A.T., Barloon, P.J., Goetz, A.F.H., 1993a. The Spectral Image Processing System (SIPS) -interactive visualization and analysis of imaging spectrometer data. *Remote Sens. Environ.* 44, 145–163.
- Kruse, F.A., Lefkoff, A.B., Dietz, J.B., 1993b. Expert system-based mineral mapping in northern Death Valley, California/Nevada, using the airborne visible/infrared imaging spectrometer (AVIRIS). *Remote Sens. Environ.* 44 (2–3), 309–336.
- Kruse, F.A., Boardman, J.W., Huntington, J.F., 2002. Comparison of airborne and satellite hyperspectral data for geologic mapping, in: *Proc. SPIE 4725, Algorithms and Technologies for Multispectral, Hyperspectral, and Ultraspectral Imagery VIII*. SPIE, Bellingham, WA, pp. 128–139.
- Kruse, F.A., Boardman, J.W., Huntington, J.F., 2003. Comparison of airborne hyperspectral data and EO-1 Hyperion for mineral mapping. *IEEE Trans. Geosci. Remote Sens.* 41 (6), 1388–1400.
- Likas, A., Vlassis, N., Verbeek, J.J., 2003. The global k-means clustering algorithm. *Pattern Recognit.* 36 (2), 451–461.
- Liu, Y., Li, Z., Xiong, H., Gao, X., Wu, J., 2010. Understanding of internal clustering validation measures, in: *Proc. 2010 IEEE International Conference on Data Mining*. IEEE, Piscataway, NJ.
- Macqueen, J., 1965. Some Methods for Classification and Analysis of MultiVariate Observations. *Proc. of Berkeley Symposium on Mathematical Statistics & Probability*.
- Mauriohooho, K., Barker, S.L.L., Rae, A., 2016. Mapping lithology and hydrothermal alteration in geothermal systems using portable X-ray fluorescence (pXRF): A case study from the Tauhara geothermal system, Taupo Volcanic Zone. *Geothermics*. 64, 125–134.

- Meer, F.V.D., 2004. Analysis of spectral absorption features in hyperspectral imagery. *Int. J. Appl. Earth Obs. Geoinf.* 5 (1), 55–68.
- Meer, F.V.D., Bakker, W., 1997. Cross correlation spectral matching: Application to surface mineralogical mapping using AVIRIS data from Cuprite, Nevada. *Remote Sens. Environ.* 61, 371–383.
- Megat Ali, M.S.A., Taib, M.N., Tahir, N.M., Jahidin, A.H., Yassin, M., 2014. EEG sub-band spectral centroid frequencies extraction based on Hamming and equiripple filters: A comparative study. in: 2014 IEEE 10th International Colloquium on Signal Processing & its Applications (CSPA). IEEE, Piscataway, NJ.
- Moore, F., Rastmanesh, F., Asadi, H., Modabberi, S., 2008. Mapping mineralogical alteration using principal-component analysis and matched filter processing in the Takab area, north-west Iran, from ASTER data. *International Journal of Remote Sensing* 29 (10), 2851–2867.
- Ouahabi, M.E., Daoudi, L., Fagel, N., 2014. Mineralogical and geotechnical characterization of clays from northern Morocco for their potential use in the ceramic industry. *Clay Miner.* 49 (1), 35–51.
- Peña, J.M., Lozano, J.A., Larrañaga, P., 1999. An empirical comparison of four initialization methods for the k-means algorithm. *Pattern Recognit. Lett.* 20, 1027–1040.
- Pour, B.A., Hashim, M., 2011. Identification of hydrothermal alteration minerals for exploring of porphyry copper deposit using ASTER data, SE Iran. *Journal of Asian Earth Sciences*. 42, 1309–1323.
- Pour, B.A., Hashim, M., 2015a. Hydrothermal alteration mapping from Landsat-8 data, Sar Cheshmeh copper mining district, south-eastern Islamic Republic of Iran. *Journal of Taibah University for Science*. 9 (2), 155–166.
- Pour, B.A., Hashim, M., 2015b. Evaluation of Earth Observing-1 (EO1) Data for Lithological and Hydrothermal Alteration Mapping: A Case Study from Urumieh-Dokhtar Volcanic Belt, SE Iran. *Journal of the Indian Society of Remote Sensing*. 43 (3), 583–597.
- Swayze, G.A., Clark, R.N., Goetz, A.F.H., Chrien, T.G., Gorelick, N.S., 2003. Effects of spectrometer band pass, sampling, and signal-to-noise ratio on spectral identification using the Tetracorder algorithm. *Journal of Geophysical Research*. 108 (E9), 5105.
- Swayze, G.A., Clark, R.N., Goetz, A.F.H., Livo, K.E., Breit, G.N., Kruse, F.A., Sutley, S.J., Snee, L.W., Lowers, H.A., Post, J.L., Stoffregen, R.E., Ashley, R.P., 2014. Mapping Advanced Argillic Alteration at Cuprite, Nevada, Using Imaging Spectroscopy. *Economic Geology* 109 (5), 1179–1221.
- Swayze, G.A., Clark, R.N., Kruse, F., Sutley, S., Gallagher, A., 1992. Ground-truthing AVIRIS mineral mapping at Cuprite, Nevada. in: Summaries of the 3rd Annual JPL Airborne Geoscience Workshop. JPL, Pasadena, CA, pp. 47–49.
- Tzortzis, G., Likas, A., 2014. The minmax k-means clustering algorithm. *Pattern Recognit.* 47 (7), 2505–2516.
- Vane, G., Goetz, A.F.H., 1993. Terrestrial imaging spectrometry: current status, future trends. *Remote Sens. Environ.* 44, 117–126.
- Vane, G., Green, R.O., Chrien, T.G., Enmark, H.T., Hansen, E.G., Porter, W.M., 1993. The airborne visible infrared imaging spectrometer (AVIRIS). *Remote Sens. Environ.* 44 (2–3), 127–143.
- Vaughan, R.G., Calvin, W.M., Taranik, J.V., 2003. SEBASS hyperspectral thermal infrared data: Surface emissivity measurement and mineral mapping. *Remote Sens. Environ.* 85 (1), 48–63.
- Wei, J., Ming, Y.F., Han, L.S., Ren, Z.L., Guo, Y.M., 2015. Method of remote sensing identification for mineral types based on multiple spectral characteristic parameters matching. *Spectrosc. Spectr. Anal.* 35 (10), 2862–2866.
- Xu, R., Wunsch, D.C., 2005. Survey of clustering algorithms. *IEEE Trans. Neural Netw.* 16 (3), 645–678.
- Xu, X., Li, J., Wu, C., Plaza, A., 2017. Regional clustering-based spatial preprocessing for hyperspectral unmixing. *Remote Sens. Environ.* 204, 333–346.